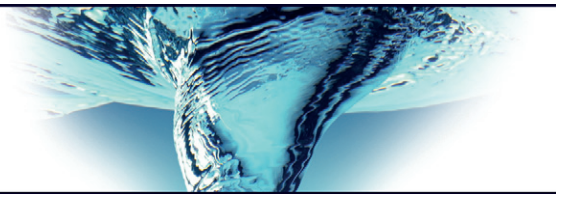
CrossMark

J. Fluid Mech. (2017), *vol.* 824, R3, doi:10.1017/jfm.2017.388



JFM RAPIDS
journals.cambridge.org/rapids

Dynamics of drop impact onto a solid sphere: spreading and retraction

Yang Zhu[1], Hao-Ran Liu[1], Kai Mu[1], Peng Gao[1], Hang Ding[1,†] and Xi-Yun Lu[1]

[1]Department of Modern Mechanics, University of Science and Technology of China, Hefei 230026, China

(Received 14 March 2017; revised 24 April 2017; accepted 26 May 2017; first published online 10 July 2017)

In this paper, drop impact onto a sphere is numerically investigated at moderate Reynolds and Weber numbers. It is naturally expected that the aspect ratio of the sphere to the drop, λ_r, would make a big difference to drop spreading and retraction on the sphere, compared with drop impact onto a flat substrate. To quantitatively assess the effect of λ_r, a diffuse-interface immersed-boundary method is adopted after being validated against experiments. With the help of numerical simulations, we identify the key regimes in the spreading and retraction, analyse the results by scaling laws, and quantitatively evaluate the effect of λ_r on the impact dynamics. We find that the thickness of the liquid film spreading on the sphere can be well approximated by $h_{L,\infty}(1+3/4\lambda_r^{-3/2})$, where $h_{L,\infty}$ represents the film thickness of drop impact on a flat substrate. At the early stage of spreading, the temporal variation of the wetted area is independent of λ_r when the time is rescaled by the thickness of the liquid film. Drops are observed to retract on the sphere at a roughly constant speed, and the predictions of theoretical analysis are in good agreement with numerical results.

Key words: contact lines, drops, thin films

1. Introduction

Impact of a drop onto a solid surface is not only commonly seen in nature, but is related to a variety of applications in industry; examples are inkjet printing (Derby 2010), surface coating (Rukosuyev, Barannyk & Oshkai 2016) and spray cooling (Zhou, Chen & Wang 2017). Spreading and retraction of the drop on the solid surfaces are the key processes in the impact dynamics, and may be accompanied by fascinating flow phenomena such as splashing (Riboux & Gordillo 2014; Stevens 2014) and bouncing (Liu *et al.* 2014); recent reviews can be found in Yarin (2006)

† Email address for correspondence: hding@ustc.edu.cn

© Cambridge University Press 2017

https://doi.org/10.1017/jfm.2017.388 Published online by Cambridge University Press

and Josserand & Thoroddsen (2016). The parameter spaces of the flow phenomena are usually described by the dimensionless groups

$$Re = \frac{\rho U_0 D}{\mu}, \quad We = \frac{\rho U_0^2 D}{\gamma} \tag{1.1a,b}$$

and the wettability of the solid surface (represented by the contact angle θ). Here, U_0 is the impact velocity, D is the diameter, and ρ, μ and γ denote the density, viscosity and surface tension of the drop respectively.

The dynamics of drop spreading and retraction has been extensively investigated for drop impact onto a flat plate (Biance, Clanet & Quere 2004; Clanet, BéGuin & Richard 2004; Bartolo, Josserand & Bonn 2005). For liquids of low viscosity, it has been experimentally observed that the early spreading is insensitive to the wettability of the solid surface. At low U_0, the radius of the wetted area varies with an inertia–capillary time scale as $r(t) \sim (\gamma D/\rho)^{1/4} t^{1/2}$ (Biance *et al.* 2004); at relatively high U_0, it varies with an inertial time scale as $r(t) \sim (U_0 D)^{1/2} t^{1/2}$ (Kim, Feng & Chun 2000), and the radius of the maximal wetted area r_{max} follows $r_{max}/D \sim We^{1/4}$ (Clanet *et al.* 2004). For drops with relatively high impact velocity, Bartolo *et al.* (2005) experimentally observed that the drop retraction is independent of the impact velocity. In particular, the retraction velocity, $\dot{r}(t)$, follows $\dot{r}(t)/r_{max} \sim (\rho D^3/\gamma)^{-1/2}$ when the inertial and capillary forces are dominant, and $\dot{r}(t)/r_{max} \sim (\mu D/\gamma)^{-1}$ when the capillary and viscous forces are dominant.

Drop impact onto more complex substrates has attracted more and more attention recently (Liu *et al.* 2015; Dressaire, Sauret & Boulogne 2016). It has been shown that the geometry of the substrate can significantly affect the impact dynamics and results in flow phenomena different from those on a flat plate. A typical example is drop impact onto a sphere of radius R, in which the aspect ratio of the sphere to the drop, $\lambda_r = 2R/D$, is expected to play an important role. At $We \sim 500$, $Re \sim O(10^4)$ and $\lambda_r \sim 1$, Rozhkov, Prunet-Foch & Vignes-Adler (2002) experimentally observed the detachment of the liquid film from the target, forming a thin and conical lamella. At similar Re and We, Bakshi, Roisman & Tropea (2007) investigated the spreading of the liquid film on the sphere surface for various values of λ_r, and suggested that the spreading dynamics could be divided into three stages: drop deformation, inertia-dominated spreading and viscosity-dominated spreading. Mitra, Sathe & Doroodchi (2013) observed drop rebound off of the sphere after impact at relatively small Re and We; later, they theoretically analysed the maximum wetted area based on energy conservation (Mitra *et al.* 2016). Irrespective of these successes in experiments, it remains unclear how the aspect ratio influences the dynamics of spreading and retraction after impact, either qualitatively or quantitatively.

In this paper, we numerically investigate the drop deposition on a sphere after impact at moderate Reynolds and Weber numbers (We ranges from 25 to 400 and $Re \sim O(10^3)$). The aim of our study is to provide a full understanding of the dynamics of the spreading and retraction on the sphere through numerical simulation and theoretical analysis. An axisymmetric diffuse-interface immersed-boundary method (Liu & Ding 2015) is used for this purpose after being validated against experiments. Based on the numerical results, we investigate flow details that are not accessible in experiments, identify the key regimes in the spreading and retraction, analyse the results by scaling laws, and quantitatively evaluate the effect of λ_r on the impact dynamics.

https://doi.org/10.1017/jfm.2017.388 Published online by Cambridge University Press

2. Methodology

We consider here a liquid drop impacting on a sphere, and investigate its dynamics using an axisymmetric diffuse-interface immersed-boundary method (Liu & Ding 2015). This method allows for simulation of incompressible multiphase flows involving rigid objects of irregular shape and moving contact lines. The liquid–gas interface is represented by the volume fraction of the liquid, C_L, the evolution of which is governed by

$$\frac{\partial C_L}{\partial t} + \nabla \cdot (\boldsymbol{u} C_L) = \frac{1}{Pe} \nabla^2 \psi, \tag{2.1}$$

where the chemical potential ψ is defined as

$$\psi = C_L^3 - 1.5C_L^2 + 0.5C_L - C_L C_S(1 - C_L - C_S) - Cn^2 \nabla^2 C_L \tag{2.2}$$

and the Cahn number Cn is a dimensionless measure of the thickness of the diffuse interface. The Péclet number is set to $Pe = 1/Cn$ (Liu & Ding 2015). To simulate the motion of contact lines on the curved substrate, a characteristic moving contact line model (Lee & Kim 2011; Liu & Ding 2015) is used to update C_L at the embedded solid objects. The distribution of the volume fraction of the solid, C_S, is prescribed according to the position of the sphere. More details of the numerical implementation can be found in Liu & Ding (2015).

The method is verified by comparing with our experiments on drop impact onto a sphere, despite the fact that the same codes have been used to simulate water entry problems and the obtained results compared favourably with experiments (Ding *et al.* 2015). The experimental set-up includes polished steel spheres of 3 mm in diameter, which are fixed on a steel needle, and droplets of size between 2 mm and 2.5 mm. The impact velocity ranges from 0.5 m s^{-1} to 1.5 m s^{-1} by adjusting the height of drop release. The impact dynamics is recorded by a high-speed camera at 1500 f.p.s. with a resolution of 1024 × 1400 pixels. The advancing contact angle is measured on a flat steel surface. The comparison between the experimental and numerical results with a mesh spacing of $\Delta x = 0.003$ is presented in figure 1. Unless otherwise stated, the interface in the simulation is represented by the $C = 0.5$ contour, and $t = 0$ corresponds to the moment when the drop comes into contact with the sphere. Clearly, a good agreement has been achieved. Figure 2 shows the grid independence study with $\Delta x = 0.002$, 0.003 and 0.005. We found that the results with $\Delta x = 0.002$ and 0.003 are virtually overlapped with respect to the drop shape at $t = 0.9$. Therefore, in the following, we use a Cartesian mesh with $\Delta x = 0.003$ in the simulations.

3. Results and discussion

3.1. *Flow features*

Typical features of interface dynamics after drop impact at moderate Reynolds and Weber numbers can be observed in figure 3, where sequences of drop shapes are shown at $Re = 1068$, $We = 144$, $\theta = 60°$ and $\lambda_r = 2.6$. At short times, the drop impact leads to high pressure at the north pole of the sphere and the occurrence of a thin layer of liquid film, which spreads out to wet the sphere. At later times ($2 \leqslant tU_0/D \leqslant 4.25$), a rim occurs near the front of liquid film. After reaching the maximum wetted area (at $tU_0/D = 4.25$), the film front retracts. In the subsequent dewetting process, the rim grows slowly by gathering the liquid in the film.

https://doi.org/10.1017/jfm.2017.388 Published online by Cambridge University Press

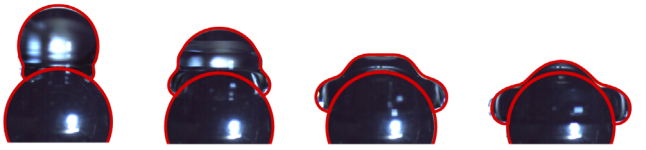


FIGURE 1. Snapshots of drop impact onto a solid sphere, in which a water drop of $D = 2.22$ mm hits a steel sphere of 3 mm in diameter at an impact velocity of $U_0 = 0.74$ m s^{-1}. The advancing contact angle $\theta_A = 95°$ in experiments. Numerical results at $We = 16.8$, $Re = 1638$, $\theta = 95°$ and $\lambda_r = 1.35$ (solid curves) are superimposed on the experimental results at dimensionless times $tU_0/D = 0.2$, 0.45, 0.9 and 1.35 (from left to right).

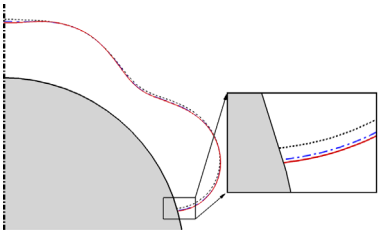


FIGURE 2. Convergence study for a drop impacting onto a sphere at $tU_0/D = 0.9$. The flow parameters are the same as in figure 1. The numerical results are obtained on meshes of different resolution: $\Delta x = 0.002$ (solid), 0.003 (dash-dotted) and 0.005 (dotted).

To quantitatively assess the effect of the aspect ratio on the impact dynamics, we performed two sets of numerical experiments, one with $Re = 1068$, $We = 144$, $\theta = 60°$ and various λ_r, and the other with $Re = 1068$, $\theta = 60°$, $\lambda_r = 2.6$ and various We. The temporal evolution of the contact line position is shown in figure 4, in terms of the azimuthal angle ξ (see figure 3*c*). Several observations can be made from these results. First, at short times ($tU_0/D \leqslant 2$), the spreading rate of the drop on the sphere, $\mathrm{d}\xi/\mathrm{d}t$, appears to be independent of We but dependent on λ_r (figure 4*b*). Second, the contact line retracts at a roughly constant speed in all cases, although the value of the speed may vary. Third, the drop is seen to oscillate on the sphere before reaching its equilibrium state, and the oscillation frequency is found to be independent of the impact velocity and λ_r. This can be interpreted by taking the drop as a spring with the coefficient of surface tension as the stiffness, which has an oscillatory period of $4\sqrt{\rho D^3/(6\gamma)}$ (Fedorchenko & Wang 2004).

3.2. *Thickness of the liquid film*

Figure 5 shows snapshots of the drop shape at $Re = 1068$, $We = 144$ and $\theta = 60°$ for various values of λ_r. For the convenience of comparison, the drop shapes are projected onto the plane with respect to $\lambda_r\beta$ and r (see the definitions of β and r in figure 3*f*), along with the results of drop impact onto a flat substrate. The results show that there are two stages of wetting, characterized by film spreading and rim development respectively. For a fixed λ_r, the thickness of the liquid film has more or less the same value in the first stage of wetting, and it is also observed that the film thickness decreases with increase of λ_r. In order to quantitatively measure it, we define the thickness of the liquid film h_L as the mean thickness at $tU_0/D = 0.5$. In

https://doi.org/10.1017/jfm.2017.388 Published online by Cambridge University Press

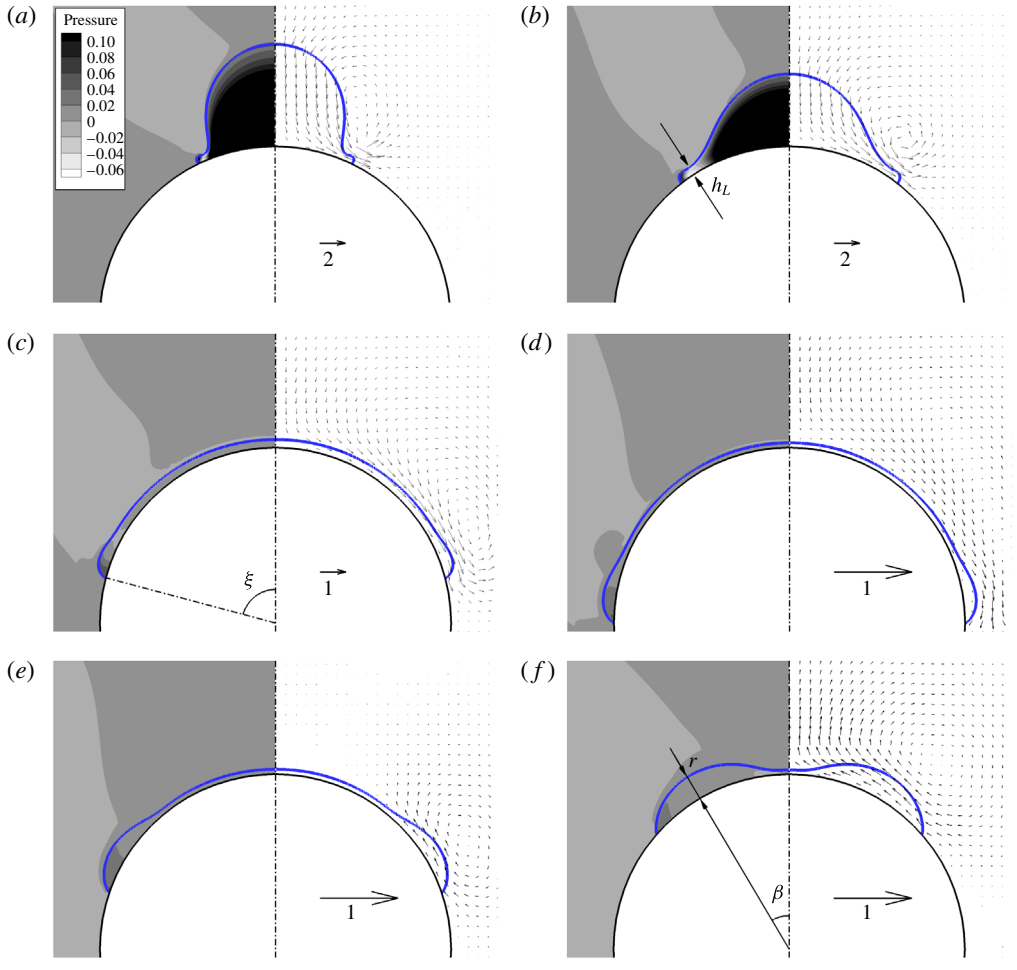


FIGURE 3. Snapshots of drop impact onto a sphere at $Re = 1068$, $We = 144$, $\lambda_r = 2.6$ and $\theta = 60°$; the dimensionless times tU_0/D from (a) to (f) correspond to 0.25, 0.5, 2, 4.25, 10 and 15 respectively. In each panel, the pressure contour (left) and velocity vectors (right) are shown, and the arrow in the sphere indicates the reference vector.

the second stage, the inertia remaining in the liquid film drives the liquid to spread, and the liquid film becomes thinner and thinner at the centre due to the lack of liquid supply; on the other hand, the spreading rate of the film is significantly hindered by the capillary force, leading to the occurrence of the rim.

Figure 6 shows the variation of h_L as a function of We in a log–log scale. We can see that the relation $h_L/D \sim We^{-1/2}$ holds for various values of λ_r. This observation is consistent with experiments on drop impact onto a flat substrate (Clanet *et al.* 2004), in which the film thickness was found to be related to the balance between the surface tension and the vertical deceleration of the impacting drop, a_D ($\sim U_0^2/D$). Similarly to the capillary length (defined as $\sqrt{\gamma/(\rho g)}$), the deformation of the drop in the impact process will have a length scale characterized by $\sqrt{\gamma/(\rho a_D)} = D/\sqrt{We}$. It is reasonable to expect that this length scale will correspond to the film thickness h_L. In this sense, the relation $h_L/D \sim We^{-1/2}$ indicates the balance between the deceleration

https://doi.org/10.1017/jfm.2017.388 Published online by Cambridge University Press

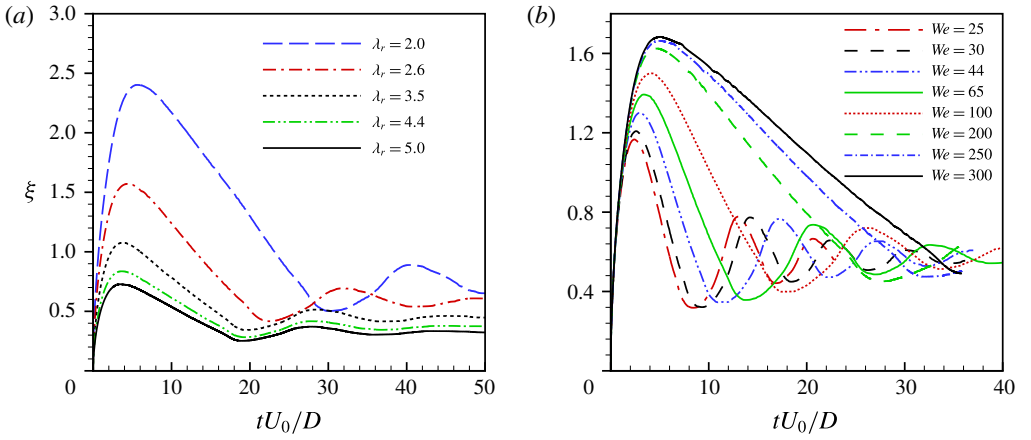


FIGURE 4. Time evolution of the angular position of the contact line in drop impact at $Re = 1068$ and $\theta = 60°$, for (*a*) $We = 144$ and various λ_r, and (*b*) $\lambda_r = 2.6$ and various We.

and the surface tension. However, h_L deviates from this relation at relatively large We, primarily because the drop impact is affected by the viscosity of the impinging liquid. To quantitatively measure the significance of the liquid viscosity, Clanet *et al.* (2004) defined an impact factor $P = We\,Re^{-4/5}$, and they experimentally found that the viscous effect played an important role when $P > 0.3$. For the cases considered here, i.e. $Re = 1068$, this suggests that the transition will occur at $We > 79$. This is consistent with our numerical simulations, and, moreover, it is interesting to see that $h_L/D \sim We^{-1/4}$ after the transition (see the inset of figure 6).

It is clear from figure 6 that h_L is dependent on λ_r. This can be understood by the fact that the smaller the sphere is, the less acceleration the drop experiences during impact, and consequently the larger h_L is. We found that the dependence can be well fitted by

$$h_L \sim h_{L,\infty}(1 + 3/4\lambda_r^{-3/2}), \tag{3.1}$$

where $h_{L,\infty}$ represents the value of h_L when $\lambda_r \to \infty$. The rescaled results for the film thickness for different values of λ_r are nearly overlapped, as shown in the inset of figure 6. Moreover, the fitting of the film thickness in (3.1) suggests that $h_{L,\infty} = 0.052D$ at $Re = 1068$, $We = 144$ and $\theta = 60°$; by contrast, the simulation of drop impact onto a flat substrate yields a rather close value, i.e. $h_{L,\infty} = 0.045D$.

3.3. *Wetting dynamics*

A scaling law is presented here to analyse the wetting dynamics dominated by the inertia of the drop. Provided that the liquid film spreads on the sphere at a rate of $R\,\mathrm{d}\xi/\mathrm{d}t$, it would require a mass flux of $\sim 2\pi\rho R^2 h_L \sin\xi\,\mathrm{d}\xi/\mathrm{d}t$ to maintain its spreading. The mass flux should be supplied by the remaining drop above the liquid film, driven by the kinetic energy of the drop. Therefore, it has order $\sim \pi D^2 \rho U_0/4$. If we assume that the mass supply does not change significantly in the early stage of wetting, mass conservation of the liquid phase suggests

$$2\lambda_r^2 h_L \sin\xi \frac{\mathrm{d}\xi}{\mathrm{d}t} \sim U_0. \tag{3.2}$$

https://doi.org/10.1017/jfm.2017.388 Published online by Cambridge University Press

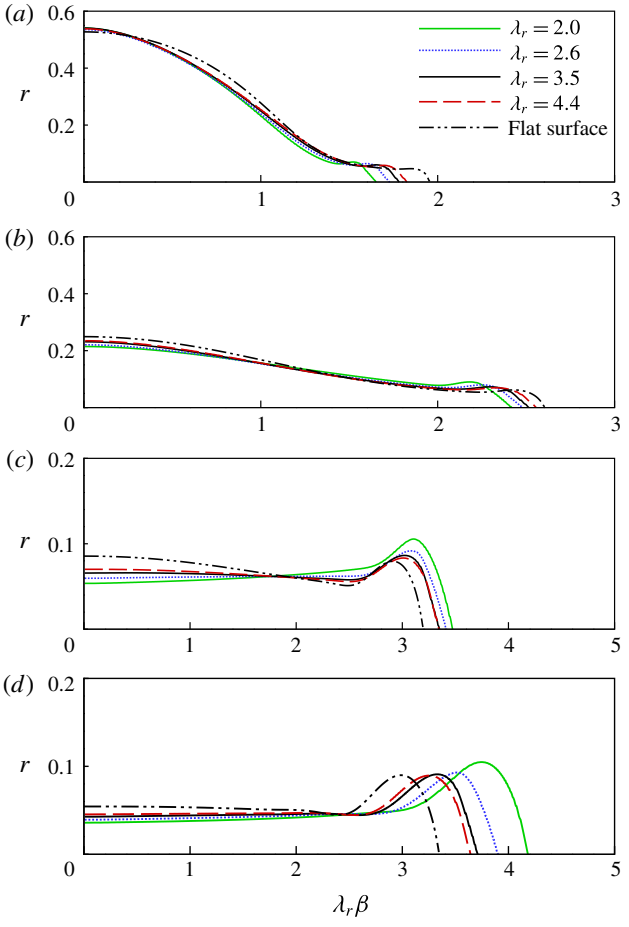


FIGURE 5. Snapshots of the drop shape at $Re = 1068$, $We = 144$ and $\theta = 60°$ for different values of λ_r. The dimensionless times tU_0/D from (*a*) to (*d*) correspond to 0.5, 1, 2 and 3 respectively.

Since h_L has a roughly uniform thickness during the impact and $h_L/D \sim 1 + 3/4\lambda_r^{-3/2}$, the integration of (3.2) from $t = 0$ yields

$$\lambda_r^2(1 - \cos\xi) \sim \frac{t\,U_0}{(1 + 3/4\lambda_r^{-3/2})D}. \tag{3.3}$$

When $h_L \ll R$, the left-hand side of (3.3) is equivalent to the dimensionless wetted area. Therefore, (3.3) states that the wetted area should increase linearly with the dimensionless time $\tau = (t\,U_0)/((1 + 3/4\lambda_r^{-3/2})D)$ at the early impact. Figure 7(*a*) shows the numerical results for the wetted area as a function of τ at $Re = 1068$, $We = 144$ and $\theta = 60°$ for various values of λ_r. It is clear that (3.3) provides a good prediction of the wetting dynamics for $\tau \leqslant 1.5$, during which the results for different values of λ_r collapse into a straight line. At $\tau = 1.5$, the drop evolves into a 'pancake' with a thickness of approximately h_L (see, e.g., figure 3*c*). The numerical results deviate from the theoretical prediction afterwards because of the invalid assumption of uniform film thickness. Figure 7(*a*) also shows that the maximal

https://doi.org/10.1017/jfm.2017.388 Published online by Cambridge University Press

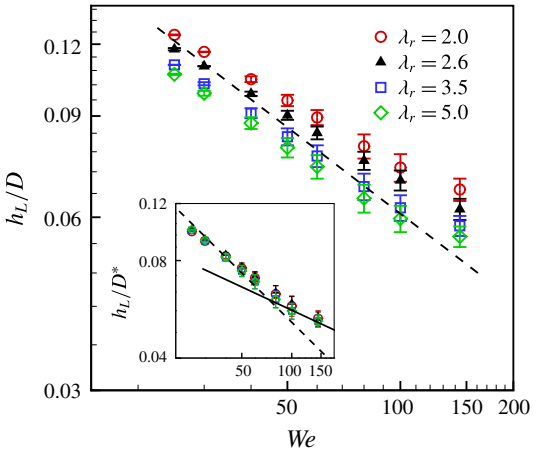


FIGURE 6. Film thickness h_L as a function of We at $Re = 1068$, $\theta = 60°$ and various values of λ_r. The dashed line denotes a slope of $1/2$. In the inset, D^* represents $(1 + 3/4\lambda_r^{-3/2})D$, and the dashed and solid lines denote slopes of $1/2$ and $1/4$ respectively.

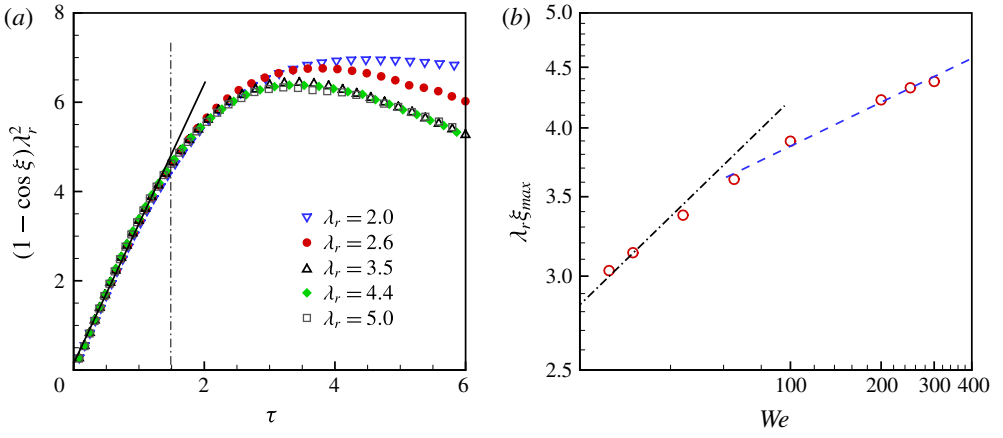


FIGURE 7. Results at $Re = 1068$ and $\theta = 60°$. (*a*) Time evolution of the wetted area in terms of $\lambda_r^2(1 - \cos\xi)$ at $We = 144$; τ denotes $tU_0/((1 + 3/4\lambda_r^{-3/2})D)$. The solid straight line represents a linear fitting and the dash-dotted line indicates the moment at which the drop evolves into a layer of liquid film of uniform thickness; see, e.g., figure 3(*c*). (*b*) The maximal wetted area (in terms of $\lambda_r\xi_{max}$) as a function of We at $\lambda_r = 2.6$. The dash-dotted and dashed lines denote slopes of $1/4$ and $1/8$ respectively.

wetted area on spheres of different sizes decreases monotonically with λ_r. Figure 7(*b*) shows the maximal wetted area (in terms of its arclength $\lambda_r\xi_{max}$) as a function of We at $Re = 1068$, $\lambda_r = 2.6$ and $\theta = 60°$. We can observe that $\lambda_r\xi_{max} \sim We^{1/4}$ for $We < 75$, and $\lambda_r\xi_{max} \sim We^{1/8}$ for $We > 75$. This can be naturally derived from mass conservation, which suggests that the maximal wetted area should be inversely proportional to the film thickness.

For small values of ξ, (3.3) can be further simplified, i.e. $\lambda_r\xi \sim (tU_0/D)^{1/2}$. Under extreme conditions such as $\lambda_r \to \infty$ (i.e. a flat substrate), this implies that the radius

https://doi.org/10.1017/jfm.2017.388 Published online by Cambridge University Press

of the wetted area, L, should satisfy $L/D \sim (tU_0/D)^{1/2}$. This is in good agreement with previous numerical studies (Kim *et al.* 2000).

3.4. *Rate of rim retraction*

In the retraction stage, the capillary force acts as the driving force to pull the rim back, while the inertia and viscosity are the resisting forces. Due to the relative significance of the two resisting forces, which can be represented by the Ohnesorge number $Oh(=\sqrt{We}/Re)$, the retraction speed may exhibit different dependence on the Weber number (Bartolo *et al.* 2005). For a drop with low viscosity, the motion of the rim can be modelled by

$$\frac{\mathrm{d}}{\mathrm{d}t}\left(mR\frac{\mathrm{d}\xi}{\mathrm{d}t}\right) = F_c, \tag{3.4}$$

where m is the mass of the rim and $F_c = 2\pi R \sin\xi(1-\cos\theta)\gamma$ is the capillary force acting on the rim. Based on the observation of a constant angular velocity of retraction $\mathrm{d}\xi/\mathrm{d}t$ (see figure 4), (3.4) can be simplified as

$$R\frac{\mathrm{d}\xi}{\mathrm{d}t}\frac{\mathrm{d}m}{\mathrm{d}t} = F_c. \tag{3.5}$$

With the assumption of a stationary liquid film (see, e.g., figure 3*d*,*e* for the velocity distribution in the film), the mass flux of the rim, $\mathrm{d}m/\mathrm{d}t$, can be approximated by $2\pi R^2 h_{min}\rho\sin\xi\,\mathrm{d}\xi/\mathrm{d}t$, where h_{min} is the film thickness when the film has the maximal wetted area (or ξ reaches its maximum value, ξ_{max}). Volume conservation suggests that $h_{min} \sim D/(\lambda_r^2(1-\cos\xi_{max}))$. Therefore, the retraction speed follows

$$\frac{\mathrm{d}\xi}{\mathrm{d}t} \sim \frac{\sqrt{(1-\cos\theta)(1-\cos\xi_{max})}}{\tau_i}, \tag{3.6}$$

where $\tau_i = \sqrt{\rho D^3/\gamma}$ is the inertial–capillary time scale. Figure 8(*a*) shows $\xi/(1-\cos\xi_{max})^{1/2}$ as a function of t/τ_i for $Oh < 0.008$. All of the numerical results appear to collapse into a single line in the retraction stage, and thus are in good agreement with the theoretical analysis in (3.6). On the other hand, $1-\cos\xi_{max}$ approaches ξ_{max}^2 when $\lambda_r \to \infty$, and thus (3.6) can be rewritten as $\dot{r}/r_{max} \sim \tau_i^{-1}$. This is consistent with the results for a flat substrate by Bartolo *et al.* (2005).

For a drop with high viscosity, the viscous effect F_v near the contact line can be modelled by a linear force–velocity relation (de Gennes 1985), such that $F_v \sim \mu R^2 \xi(\mathrm{d}\xi/\mathrm{d}t)$. Therefore, the balance between F_v and F_c yields

$$\frac{\mathrm{d}\xi}{\mathrm{d}t} \sim \frac{(1-\cos\theta)\sin\xi}{\lambda_r\xi}\tau_v^{-1}, \tag{3.7}$$

where $\tau_v = \mu D/\gamma$ is the viscous–capillary time scale. Figure 8(*b*) shows the numerical results for drop retraction with $Oh > 0.013$, in terms of $\xi\,\xi_{max}/\sin\xi_{max}$ versus the time t/τ_v. We can observe that the results are roughly parallel to each other in the retraction stage, suggesting that (3.7) gives a good prediction of the rim retraction in the viscous–capillary regime.

https://doi.org/10.1017/jfm.2017.388 Published online by Cambridge University Press

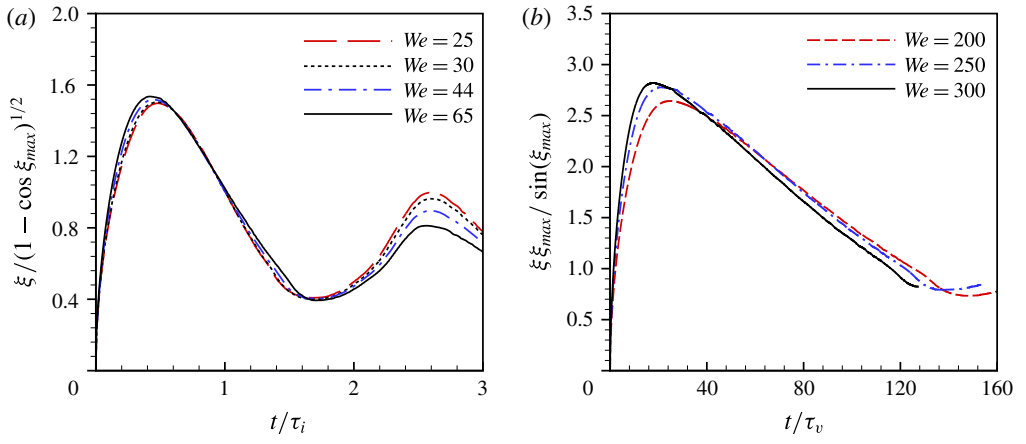


FIGURE 8. (*a*) Inertial–capillary retraction at $Oh < 0.008$, in terms of ξ rescaled by $(1-\cos\xi_{max})^{1/2}$ versus t/τ_i, and (*b*) viscous–capillary retraction at $Oh > 0.013$, in terms of ξ rescaled by $\sin\xi_{max}/\xi_{max}$ versus t/τ_v.

4. Conclusion

Drop impact onto a sphere was numerically investigated at moderate Reynolds and Weber numbers using a diffuse-interface immersed-boundary method, with the aim of providing a quantitative evaluation of the effect of λ_r on the dynamics of drop spreading and retraction. Based on the numerical results, it was found that the thickness of the liquid film, h_L, can be well approximated by $h_L \sim h_{L,\infty}(1+3/4\lambda_r^{-3/2})$. The variation of h_L with the Weber number appears to have two scaling laws, $h_L/D \sim We^{-1/2}$ for $Oh < 0.008$ and $h_L/D \sim We^{-1/4}$ for $Oh > 0.008$, primarily due to the viscous effect becoming significant at relatively large Oh. It is very interesting to see that coincidentally at roughly the same parameters ($Oh \approx 0.008$ or $We \approx 75$ and $Re = 1068$), the regime transition also occurs in the drop retraction and the maximal wetting area when varying the Weber number. At the early stage of spreading, the temporal variation of the wetted area was shown to be independent of λ_r when the time was rescaled by the thickness of the liquid film, due to the fact that the impact inertia is dominant during that period. The retraction rates were theoretically analysed by taking λ_r into account, and the theoretical prediction was consistent with the numerical results.

Acknowledgements

The authors are grateful for the support of the National Natural Science Foundation of China (grant nos. 11425210, 11621202, 11672288), the Chinese Academy of Sciences (grant no. XDB22040103) and the Fundamental Research Funds for the Central Universities.

References

BAKSHI, S., ROISMAN, I. V. & TROPEA, C. 2007 Investigations on the impact of a drop onto a small spherical target. *Phys. Fluids* **19**, 032102.

BARTOLO, D., JOSSERAND, C. & BONN, D. 2005 Retraction dynamics of aqueous drops upon impact on non-wetting surfaces. *J. Fluid Mech.* **545**, 329–338.

https://doi.org/10.1017/jfm.2017.388 Published online by Cambridge University Press

BIANCE, A. L., CLANET, C. & QUERE, D. 2004 First steps in the spreading of a liquid droplet. *Phys. Rev.* E **69**, 016301.

CLANET, C., BÉGUIN, C. & RICHARD, D. 2004 Maximal deformation of an impacting drop. *J. Fluid Mech.* **517**, 199–208.

DERBY, B. 2010 Inkjet printing of functional and structural materials: fluid property requirements, feature stability, and resolution. *Annu. Rev. Mater. Res.* **40**, 395–414.

DING, H., CHEN, B. Q., LIU, H. R., ZHANG, C. Y., GAO, P. & LU, X. Y. 2015 On the contact-line pinning in cavity formation during solid–liquid impact. *J. Fluid Mech.* **783**, 504–525.

DRESSAIRE, E., SAURET, A. & BOULOGNE, F. 2016 Drop impact on a flexible fiber. *Soft Matt.* **12**, 200–208.

FEDORCHENKO, A. I. & WANG, A. B. 2004 The formation and dynamics of a blob on free and wall sheets induced by a drop impact on surfaces. *Phys. Fluids* **16**, 3911–3920.

DE GENNES, P. G. 1985 Wetting: statics and dynamics. *Rev. Mod. Phys.* **57**, 827–863.

JOSSERAND, C. & THORODDSEN, S. T. 2016 Drop impact on a solid surface. *Annu. Rev. Fluid Mech.* **48**, 365–391.

KIM, H. Y., FENG, Z. C. & CHUN, J. H. 2000 Instability of a liquid jet emerging from a droplet upon collision with a solid surface. *Phys. Fluids* **12**, 531–541.

LEE, H. G. & KIM, J. 2011 Accurate contact angle boundary conditions for the Cahn–Hilliard equations. *Comput. Fluids* **44**, 178–186.

LIU, H. R. & DING, H. 2015 A diffuse-interface immersed-boundary method for two-dimensional simulation of flows with moving contact lines on curved substrates. *J. Comput. Phys.* **294**, 484–502.

LIU, Y. H., ANDREW, M., LI, J., YEOMANS, J. M. & WANG, Z. K. 2015 Symmetry breaking in drop bouncing on curved surfaces. *Nat. Commun.* **6**, 10034.

LIU, Y. H., MOEVIUS, L., XU, X. P., QIAN, T., YEOMANS, J. M. & WANG, Z. K. 2014 Pancake bouncing on superhydrophobic surfaces. *Nat. Phys.* **10**, 515–519.

MITRA, S., NGUYEN, T. B. T., DOROODCHI, E., PAREEK, V., JOSHI, J. B. & EVANS, G. M. 2016 On wetting characteristics of droplet on a spherical particle in film boiling regime. *Chem. Engng Sci.* **149**, 181–203.

MITRA, S., SATHE, M. J. & DOROODCHI, E. 2013 Droplet impact dynamics on a spherical particle. *Chem. Engng Sci.* **100**, 105–119.

RIBOUX, G. & GORDILLO, J. M. 2014 Experiments of drops impacting a smooth solid surface: a model of the critical impact speed for drop splashing. *Phys. Rev. Lett.* **113**, 024507.

ROZHKOV, A., PRUNET-FOCH, B. & VIGNES-ADLER, M. 2002 Impact of water drops on small targets. *Phys. Fluids* **14**, 3485–3501.

RUKOSUYEV, M. V., BARANNYK, O. & OSHKAI, P. 2016 Design and application of nanoparticle coating system with decoupled spray generation and deposition control. *J. Coat Technol. Res.* **13**, 769–779.

STEVENS, C. S. 2014 Scaling of the splash threshold for low-viscosity fluids. *Eur. Phys. Lett.* **106**, 24001.

YARIN, A. L. 2006 Drop impact dynamics: splashing, spreading, receding, bouncing . . . . *Annu. Rev. Fluid Mech.* **38**, 159–192.

ZHOU, Z. F., CHEN, B. & WANG, R. 2017 Comparative investigation on the spray characteristics and heat transfer dynamics of pulsed spray cooling with volatile cryogens. *Exp. Therm. Fluid Sci.* **82**, 189–197.

https://doi.org/10.1017/jfm.2017.388 Published online by Cambridge University Press